Unravelling the development of preferred crystallographic orientation in dual-phase amorphous/nanocrystalline Zr-V thin films

A. Borroto, E. Chaslin, S. Bruyere, Z. Fernández-Gutiérrez, Q. Liebgott, J.-F. Pierson, D. Horwat

Journal of Alloys and Compounds 1006 (2024) 176270

Contents lists available at ScienceDirect

Journal of Alloys and Compounds

journal homepage: www.elsevier.com/locate/jalcom

Unravelling the development of preferred crystallographic orientation in dual-phase amorphous/nanocrystalline Zr-V thin films

A. Borroto [a,b,*], E. Chaslin [b], S. Bruyère [a], Z. Fernández-Gutiérrez [a], Q. Liebgott [a], J.F. Pierson [a], D. Horwat [a,*]

[a] Université de Lorraine, CNRS, IJL, Nancy F-54000, France
[b] Univ Rennes, CNRS, IETR-UMR 6164, Rennes F-35000, France

ARTICLE INFO

Keywords:
Zr-V alloys
Dual-phase alloys
Amorphous-nanocrystalline thin films
Preferred crystallographic orientation
Pole figures

ABSTRACT

Dual-phase amorphous/nanocrystalline alloys have been proven to present enhanced properties compared to their amorphous or nanocrystalline single-phase counterparts. These dual-phase materials are typically composed of nanocrystalline cores embedded in an amorphous matrix. In contrast, a new kind of dual-phase metallic films has recently been reported in which cone-shaped crystalline regions evolve as a result of competitive growth between the amorphous and crystalline phases with increasing film thickness. Here, we demonstrate that, unlike typical dual-phase alloys, Zr-V thin films exhibiting crystalline/amorphous competitive growth develop a preferred crystallographic orientation upon growth. Relying on pole figure observations, we uncover the development of a preferred orientation of the (110) crystallographic planes in the growth direction of the film with increasing film thickness. High-resolution transmission electron microscopy analysis reveals that the crystalline regions are formed by nano-branches which grow (110)-oriented. Based on this result, together with scanning and transmission electron microscopy observations, we associate the development of the thickness-dependent preferred orientation to the impingement between cone-shaped crystalline regions. This process triggers a selective growth mechanism that favors the selection of nano-branches growing near the direction of film growth. Our results and analyses provide a step forward in understanding the growth kinetics of dual-phase alloys presenting complex microstructures.

1. Introduction

Combining both amorphous and nanocrystalline metallic phases in the same alloy has proven to be an effective strategy to obtain dual-phase materials with improved properties compared to their amorphous or nanocrystalline single-phase counterparts [1]. For example, Wu *et al.* demonstrated that near-ideal strength at room temperature can be achieved in a dual-phase magnesium-alloy thin film consisting of uniformly distributed $MgCu_2$ nanocrystals embedded in magnesium-enriched amorphous shells [2]. Wu *et al.* also demonstrated ultrahigh strength and large plasticity in a dual-phase alloy composed of crystalline Al nanograins surrounded by nano-sized metallic glass shells [3]. Furthermore, Ming *et al.* showed enhanced strength and ductility in a TiZr-based alloy formed by crystalline TiZr-rich and amorphous CuZr-rich phases [4]. In addition to improved mechanical properties, Li *et al.* reported superior comprehensive soft magnetic properties in a dual-phase amorphous/nanocrystalline FeCo-based alloy [5]. Moreover, Wang *et al.* showed unexpected thermal stability in a dual-phase $Al_{0.74}Mo_{0.26}$ alloy film formed by Al_3Mo nano-grains uniformly dispersed in the Al-Mo amorphous matrix and prepared by annealing-induced crystallization [6]. From a microstructural point of view, in most cases, dual-phase alloys are composed of nanocrystallites uniformly dispersed in the amorphous matrix. Another type of dual-phase amorphous/nanocrystalline alloys can also be obtained through grain boundary amorphization in nanocrystalline metals. This formation of a so-called amorphous intergranular film at the grain boundaries, which is produced mainly by annealing-induced solute segregation, has been shown to improve the thermal stability and mechanical properties of the alloy [7,8]. Overall, amorphous/nanocrystalline metal alloys are intrinsically polycrystalline with randomly-oriented crystallites, and a preferred crystallographic orientation in these dual-phase materials has not been reported so far.

A new kind of dual-phase metallic films consisting of nanocrystalline regions of conical shape heterogeneously distributed in an amorphous

* Corresponding authors at: Université de Lorraine, CNRS, IJL, Nancy F-54000, France.
E-mail addresses: alejandro.borroto@univ-rennes.fr (A. Borroto), david.horwat@univ-lorraine.fr (D. Horwat).

https://doi.org/10.1016/j.jallcom.2024.176270
Received 27 June 2024; Received in revised form 21 August 2024; Accepted 30 August 2024
Available online 31 August 2024

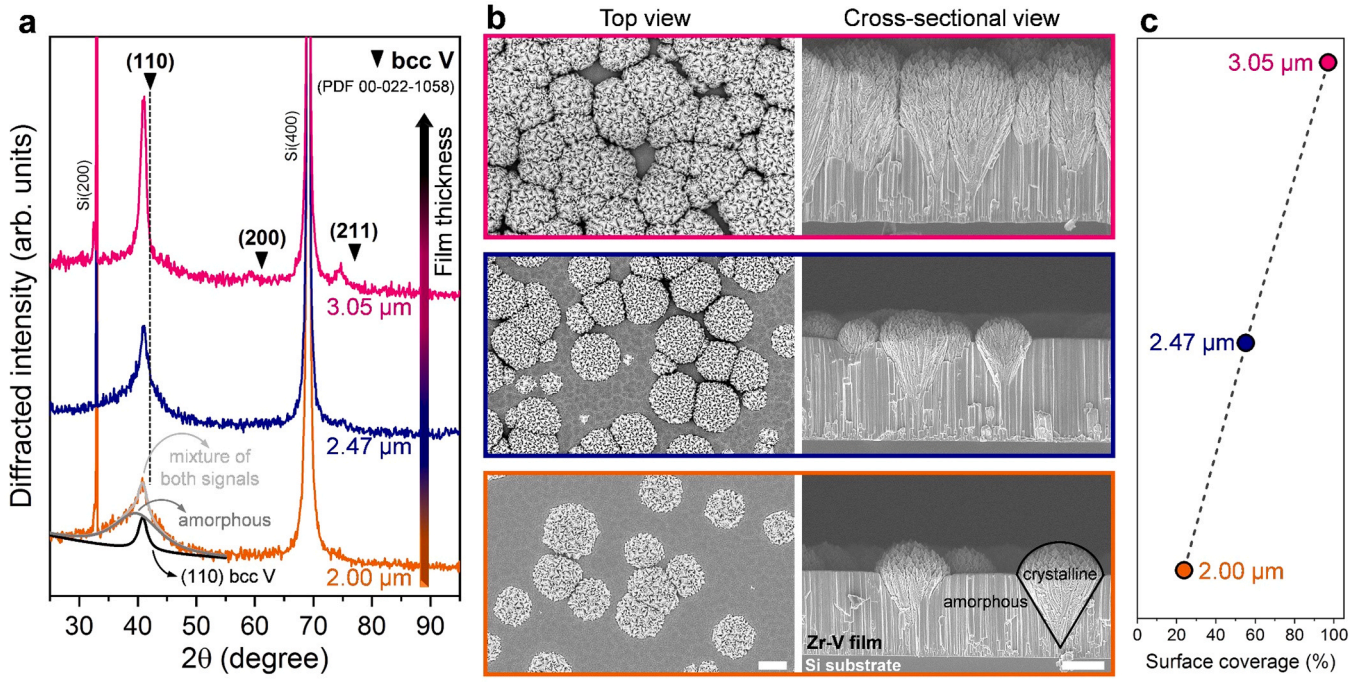

Fig. 1. Thickness-dependent microstructural evolution of Zr-V thin films exhibiting crystalline/amorphous competitive growth. (a) X-ray diffractograms of 2.00, 2.47, and 3.05 μm thick Zr-V films with 83 at% V. As the film thickness increases, the diffracted intensity associated with the bcc phase of V increases, evidencing the overgrowth of the amorphous phase by the crystalline one. (b) Top and cross-sectional view SEM images of the films showing their microstructural evolution with increasing thickness. Scale bar: 1 μm. (c) Evolution of coverage of the film surface by the crystalline regions with increasing thickness.

matrix has been recently obtained by magnetron sputtering. This dual-phase microstructure has been reported in some binary Zr-X alloys (X = Mo [9], W [10–12], Cr [13] and V [13]), and also in Ti-Al [14] thin films. In these alloys, a competitive growth between the crystalline and amorphous phases occurs with increasing film thickness, which induces a progressive overgrowth of the amorphous phase by the crystalline one. Thus, the ratio between the amorphous and crystalline phases can be tuned by using the film thickness as a control parameter. The particular microstructure of metallic films presenting nanocrystalline/amorphous competitive growth provides an avenue to manipulate their surface-related properties, as demonstrated for the optical reflectivity of Zr-Mo and Zr-W alloys [9,10]. We point-out here that, as has been proven in the case of Zr-W [10] and Zr-Cr [13] thin films, nanocrystalline/amorphous competitive growth occurs in a narrow range of alloy chemical compositions, which may be hindering the detection of this phenomenon in other metallic systems. Interestingly, prior to the discovery of nanocrystalline/amorphous competitive growth in metallic films, similar dual-phase microstructures have been reported punctually in some nitrides and oxides such as Al-N [15], Ti-O [16] and $BaTiO_3$ [17]. Another non-metallic system that exhibits this particular dual-phase microstructure is hydrogenated silicon (Si:H) synthesized by plasma-enhanced CVD, which has widely been studied because of its implication in solar cell technologies [18–20].

The marked microstructural difference between typical dual-phase amorphous/nanocrystalline alloys and dual-phase metallic films exhibiting nanocrystalline/amorphous competitive growth may trigger distinctive structural features in the latter. In particular, the overgrowth of the amorphous phase by the crystalline one could induce a significant structural change in these metallic films, such as the development of a preferred crystallographic orientation, so far elusive in typical dual-phase amorphous/nanocrystalline alloys. In the present work, we aim to unravel this question. To do so, we rely on Zr-V alloys as a model system in which nanocrystalline/amorphous competitive growth has already been observed [13]. This system has also been explored as a non-evaporable getters for achieving ultra-high vacuum conditions [21–27].

2. Experimental details

2.1. Thin film synthesis

Dual-phase amorphous/nanocrystalline Zr-V thin films were obtained by DC magnetron co-sputtering of Zr and V metallic targets in an argon atmosphere. The alloys were deposited on Si(100) single crystal substrates of 1.5×1.5 cm^2 and without external heating. To guarantee homogeneity of the films the depositions were done with the substrate holder in rotation mode. A target-to-substrate distance of 9 cm was fixed for all the experiments [10,11]. Prior to deposition, the sputtering chamber was pumped down to a base vacuum of 10^{-6} Pa using mechanical and turbo-molecular pumps. The working-gas pressure was set at 2 Pa. Discharge currents of 0.15 and 0.62 A were applied to the Zr and V targets, respectively (target dimensions: 50.8 mm in diameter, 3 mm-thick and purity higher than 99.9 %, both were powered by a Maxim 1000 DC generator). Under these conditions, Zr-V films with 83 at% V were obtained, close to the previously reported composition (86 at% V) to obtain amorphous/nanocrystalline competitive growth in this system [13]. The films thickness was controlled by adjusting the deposition time.

2.2. Thin film characterization

X-ray diffraction measurements were conducted in monochromatic parallel beam configuration with $K_{\alpha 1}Cu$ radiation (λ=1.5406 Å) using a Rigaku SmartLab diffractometer. Top and cross-section views of the films were obtained by scanning electron microscopy (SEM) using a ZEISS Gemini SEM 500 equipped with a field emission gun at an accelerating voltage of 2.0 kV. The film thickness was measured using the cross-sectional SEM images. Transmission electron microscopy (TEM) analyses were performed using a JEOL-ARM 200 Cold FEG TEM/STEM operating at 200 kV and equipped with two spherical aberration

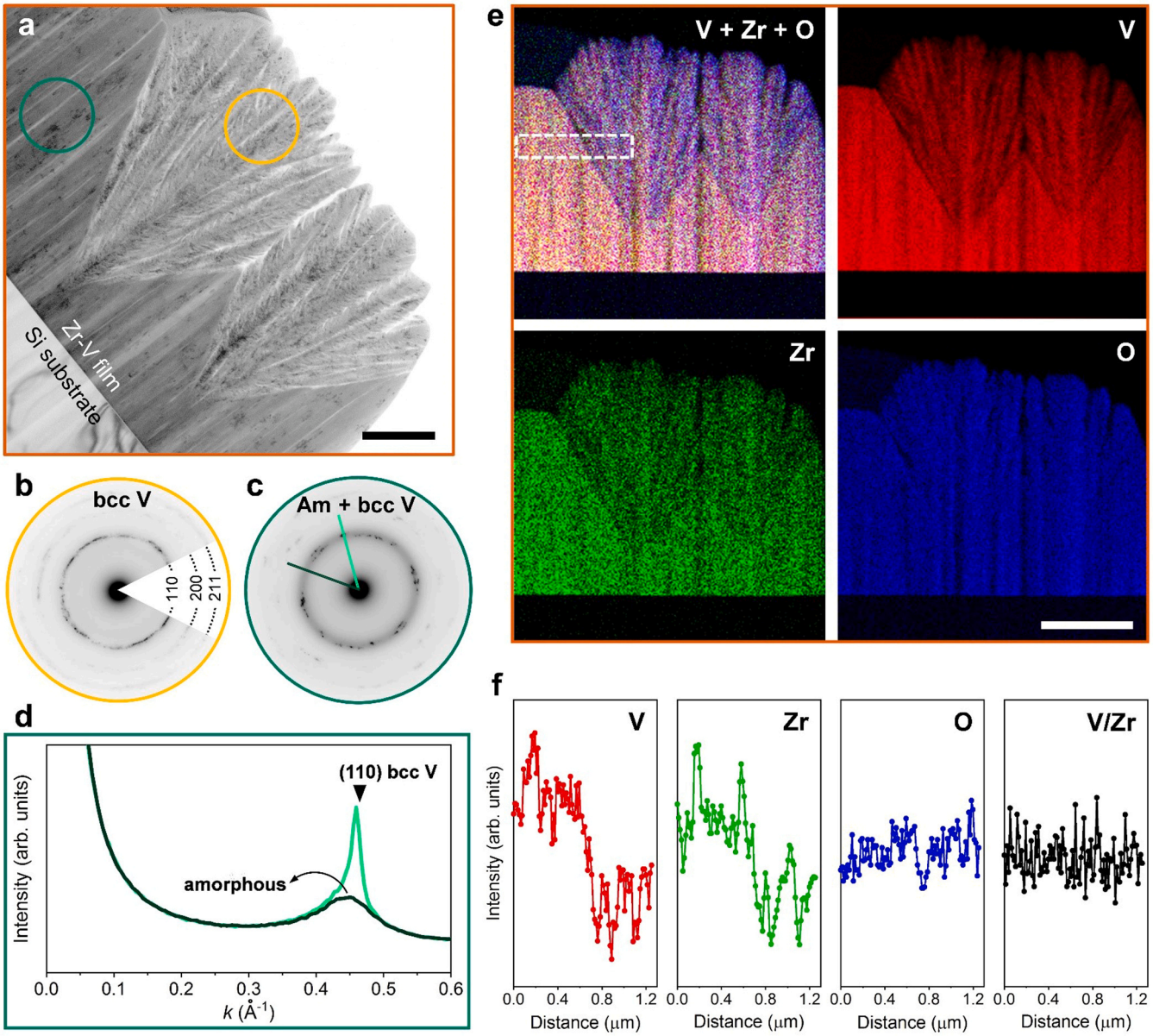

Fig. 2. Structural and chemical composition analysis of Zr-V film exhibiting crystalline/amorphous competitive growth. (a) Brigth-field TEM image of a 2.00 μm thick Zr-V film with 83 at% V. Scale bar: 500 nm. The darker-contrast zones in the columnar region reveal the presence of nanocrystals in this region. (b) SAED pattern performed on the zone marked with a yellow circle in (a) showing the polycrystalline nature of the cone-shaped regions. (c) SAED pattern performed on the zone marked with a green circle in (a) revealing the dual-phase amorphous/crystalline nature of the columnar region. (d) Intensity profiles extracted from the directions highlighted in the SAED pattern shown in (c). (e) EDS mappings showing the superposition of the V, Zr, and O signals (top-left image), and the distribution of each element. Scale bar: 1 μm. (f) Intensity profiles extracted from the highlighted area on the overlaid EDS mapping.

(Cs) probe correctors (point resolution 0.12 nm in TEM mode and 0.078 nm in STEM mode). For these analyses, a cross-section TEM sample of a 2.00 μm thick Zr-V film was prepared using a focused ion beam (FIB)-scanning electron microscope dual beam system (FEI Helios NanoLab 600i).

3. Results and discussion

3.1. Nanocrystalline/amorphous competitive growth in Zr-V thin films

X-ray diffraction and SEM analyses performed on Zr-V films with 83 at% V reveal the occurrence of crystalline/amorphous competitive growth in this system (Fig. 1). The dual-phase structure of the alloy is evidenced in the X-ray diffractogram of the 2.00 μm thick film (Fig. 1a). At this thickness, the diffractogram shows a mixture of the amorphous and crystalline signals. The broad hump is characteristic of the amorphous phase while the crystalline phase is characterized by a well-defined diffraction peak which can be associated with the (110) planes of the bcc phase of V (PDF 00–022–1058). We note that the (110) peak is shifted with respect to pure V. Its position corresponds to an interplanar distance ($d_{110}^{\text{X-ray}} = 0.221$ nm) greater than that of pure V ($d_{110}^{\text{pure-V}} = 0.214$ nm), which is due to the incorporation of Zr atoms with a larger radius than V (Zr metallic radius = 0.158 nm and V metallic radius = 0.134 nm [28]). We point-out that the stable equilibrium phase diagram of the Zr-V system predicts (at room temperature and 83 at% V) the formation of bcc-V of limited solubility and an intermetallic C15 Laves phase (ZrV_2) [29]. Hence, our results highlight the possibility of obtaining metastable phases (amorphous and supersaturated solid solution of Zr into bcc-V) due to high quenching rates associated with the

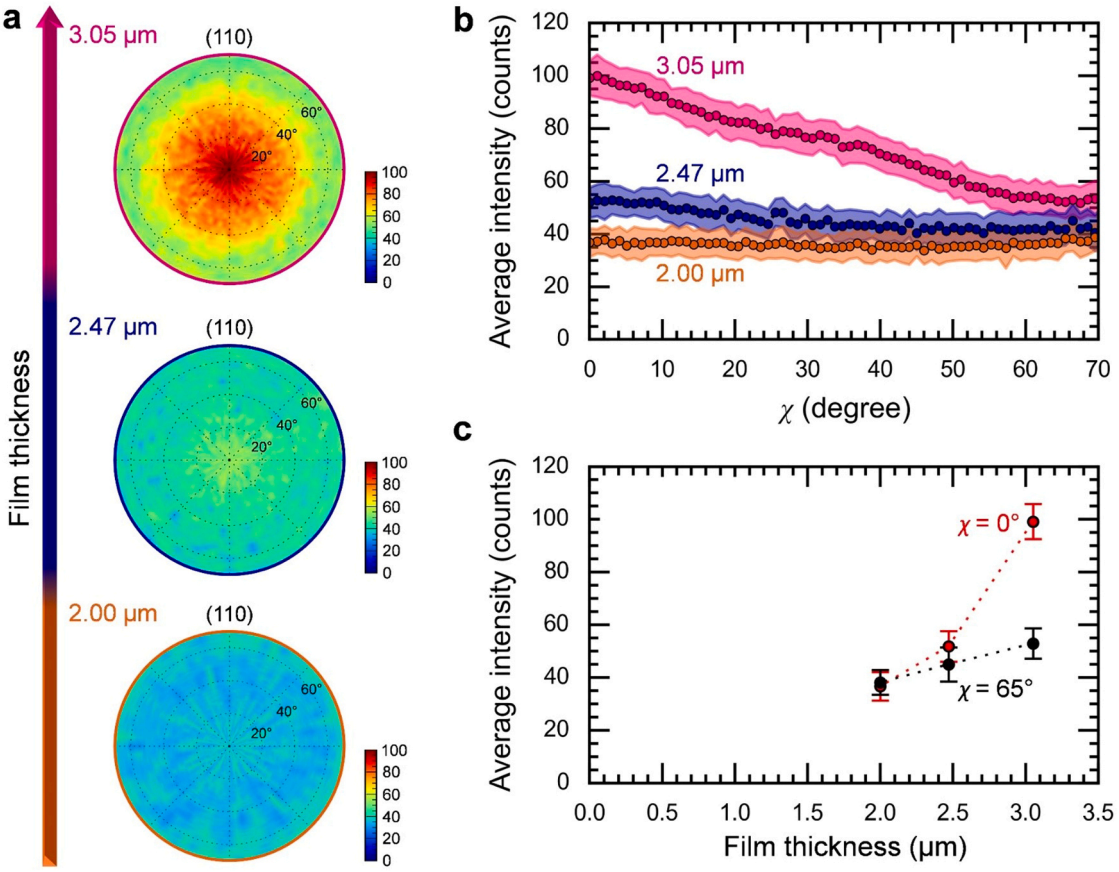

Fig. 3. Thickness-dependent development of a preferred crystallographic orientation in Zr-V thin films exhibiting crystalline/amorphous competitive growth. (a) (110) pole figures of 2.00, 2.47, and 3.05 μm thick Zr-V films with 83 at% V. (b) Average intensity profiles determined as the average diffracted intensity after a complete rotation (360°) of the film at a given χ value. (c) Evolution with film thickness of the average intensity at $\chi = 0°$ and $\chi = 65°$.

vapor condensation inherent to the magnetron sputtering process. Top and cross-sectional SEM views show the peculiar microstructure of the film, formed by two regions with different and well-defined morphologies (Fig. 1b). The crystalline regions exhibit a rounded shape from the top view and a conical shape terminated in a dome from the cross-sectional view. The amorphous region surrounds the crystalline ones and presents a columnar microstructure from the cross-sectional view, which is typical for zone I-type growth according to structure zone models [30,31].

X-ray diffractograms show that the diffracted intensity associated with the crystalline phase increases with increasing film thickness (Fig. 1a). This is in line with the SEM observations showing that, due to the conical shape of the crystalline regions, they progressively overgrow the amorphous matrix (Fig. 1b). As a result of this competitive growth between the two regions, the ratio between the crystalline and amorphous phases increases with film thickness, leading to an increased coverage of the film surface by the crystalline regions (Fig. 1c). Consequently, the surface of the 3.05 μm thick film is almost completely covered by the crystalline phase (see Liebgott *et al.* [13] for details on SEM image processing for the extraction of surface coverage by crystalline regions).

Cross-sectional transmission electron microscopy (TEM) analysis performed on the 2 μm thick Zr-V film provide details on the structure, microstructure and chemical composition of these dual-phase alloys (Fig. 2). The selected-area electron diffraction (SAED) pattern of the cone-shaped region shows well-defined rings that can be associated with bcc-V, confirming its crystalline structure (Fig. 2b). On the other hand, the SAED pattern of the columnar region shows the overlapping of a diffuse ring and some dark spots (Fig. 2c). The diffuse ring confirms the amorphous nature of this region. However, the dark spots indicate the presence of nanocrystals embedded in the amorphous matrix, revealing that the columnar region is not fully-amorphous. The intensity profiles (Fig. 2d) extracted from the directions highlighted in the SAED pattern (light and dark green lines) evidence the dual-phase character of the columnar region. In addition, the interplanar distance corresponding to the position of the dark spots can be associated with the (110) planes of bcc V, showing that the structure of the nanocrystals is the same as that of the conical regions. The presence of these nanocrystals is also observed in the bright-field TEM image of Fig. 2a. Indeed, the darker-contrast zones embedded in the amorphous nanocolumns reveal either the presence of diffracting domains or heavier Zr-rich precipitates. However, the energy-dispersive X-ray spectroscopy (EDS) mappings (Fig. 2e) demonstrate chemical homogeneity in the columnar region, disregarding the presence of precipitates and confirming the diffracting nature of the darker-contrast zones in the bright-field TEM image.

The EDS mappings also indicate a decrease in the intensity of the V and Zr signals in the fully-crystalline conical regions compared to their intensities in the columnar region, pointing to a lower atomic content of both elements in the former. On the other hand, the oxygen signal appears to be nearly homogeneous throughout the film (conical and columnar regions). These observations are confirmed by the intensity profiles (Fig. 2f) extracted from the highlighted area on the overlaid EDS mapping. Nevertheless, the intensity profiles also reveal that the ratio between the V and Zr signals does not change when passing from the columnar to the conical region. These results demonstrate, firstly, that the ratio between V and Zr content is the same in both conical and columnar regions, as also reported in the case of the Zr-Cr system exhibiting nanocrystalline/amorphous competitive growth [13]. Secondly, the porosity of the conical regions is larger than that of the columnar ones, as evidenced by the decrease in the intensity of the V and

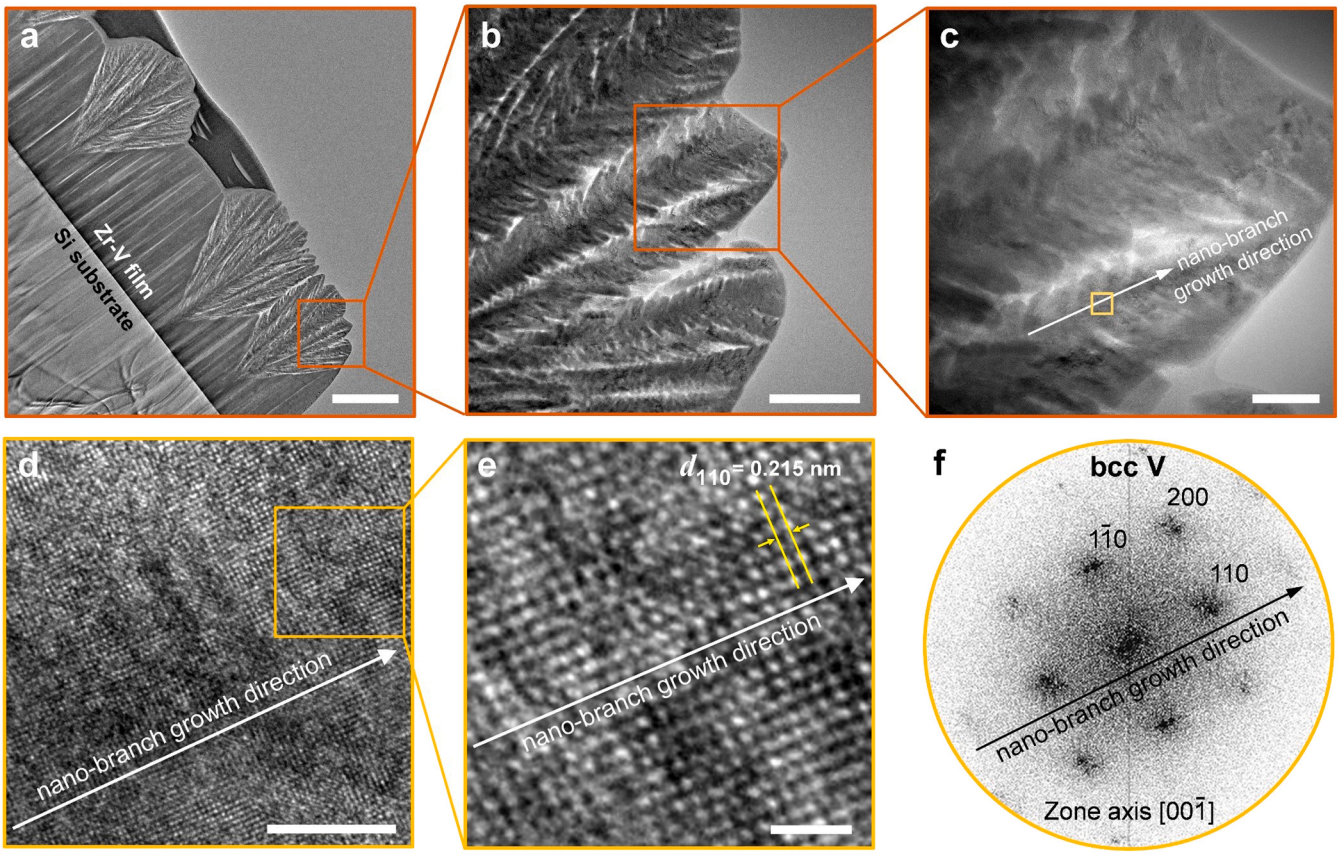

Fig. 4. High-resolution TEM analysis of Zr-V film exhibiting crystalline/amorphous competitive growth. (a) Cross-sectional TEM image of a 2.00 μm thick Zr-V film with 83 at% V. Scale bar: 1 μm. (b-c) Zooms of a cone-shaped crystalline region highlighting its particular microstructure. Scale bars: 200 nm (b) and 50 nm (c). (d-e) High-resolution TEM images from the core of a nano-branch, marked with a yellow square in (c). The white arrow, parallel to the one shown in (c), indicates the growth direction of the selected nano-branch. Scale bars: 5 nm (d) and 1 nm (e). (f) FFT of the image shown in (d). The FFT indicates that the nano-branch is growing with the (110) crystallographic planes normal to its growth direction, indicated by the black arrow.

Zr signals in this region. This is supported by the presence of clearly visible voids between the nano-branches forming the conical regions (Fig. 2e). Finally, the opened morphology of the conical regions is favorable to the penetration of oxygen and trigger surface oxidation as suggests the composite V + Zr + O color map of Fig. 2e. We note that the oxygen detected in the films is the result of their natural oxidation due to exposure to the atmosphere, and that no oxidation process was carried out on the films. Hence, the obtained microstructure could be of interest for non-evaporable getter applications.

We note that in the case of other dual-phase metallic films exhibiting nanocrystalline/amorphous competitive growth, the columnar region has been reported as fully-amorphous and the presence of nanocrystals has not been detected so far. In the following, we will use the term amorphous when referring to the region of columnar microstructure, but it is important to have in mind that this zone is not fully-amorphous in the case of the Zr-V system. Actually, the microstructure of this region resembles that of typical dual-phase alloys, composed of nanocrystallites dispersed in the amorphous matrix.

3.2. *Preferred crystallographic orientation in dual-phase Zr-V thin films*

The crystalline/amorphous competitive growth herein presented, results in the development with film thickness of a preferred crystallographic orientation. This is illustrated by the pole figures performed on the (110) reflection (Fig. 3). We note that the color scale of the pole figures indicates the intensity detected at a certain sample orientation and is proportional to the volume fraction of crystallites with their (110) crystallographic planes in reflection geometry. The pole figure of the 2.00 μm thick film (Fig. 3a) shows a nearly constant intensity regardless of the sample orientation, indicating that the alloy is polycrystalline with the (110) crystallographic planes uniformly distributed, i.e. without a preferred orientation. This is also illustrated in Fig. 3b, which shows the variation with χ of the average diffracted intensity after a complete rotation (360°) around the direction normal to the film surface. χ corresponds to the angle between the growth direction of the film (normal to the substrate surface) and the bisector between the incident and diffracted beams.

As the film thickness increases to 2.47 μm, the diffracted intensity increases compared to that of the 2.00 μm thick film (Fig. 3a-b), evidencing a higher volume fraction of crystallites (110)-oriented. This is in accordance with the increase of cone-shaped crystalline regions and corresponding increase in surface coverage of the films by these regions observed in the SEM images (Fig. 1b-c). We point-out here that both the intensity in the pole figure (Fig. 3a) and the average intensity (Fig. 3b) show a slight increase around $\chi = 0°$, revealing the onset of a preferred orientation of the (110) planes in the growth direction of the film. Finally, the 3.05 μm thick film shows a noticeable increase in diffracted intensity when approaching to $\chi = 0°$. This indicates a continuous increase in the volume fraction of (110)-oriented crystallites when approaching the growth direction of the film, highlighting the development of a preferred crystallographic orientation in this direction. This development of a preferred crystallographic orientation with increasing film thickness is clearly illustrated in Fig. 3c, which shows the evolution of the average diffracted intensity at $\chi = 0°$ and $\chi = 65°$. At $\chi = 65°$ the average intensity increases linearly with film thickness. In contrast, at $\chi = 0°$, the average intensity evolves superlinearly with film thickness,

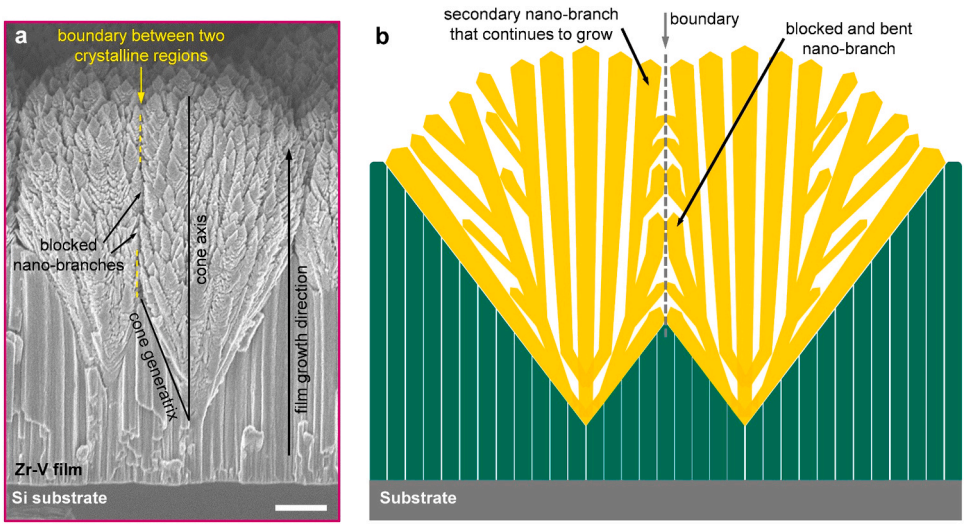

Fig. 5. Selective growth mechanism of nano-branches in Zr-V films exhibiting crystalline/amorphous competitive. (a) Cross-sectional SEM image of a 3.05 μm thick Zr-V film which highlights the blocked nano-branches at the boundary between two crystalline regions. Scale bar: 500 nm. (b) Schematic showing the different mechanisms leading to the development of a preferred orientation of the nano-branches in the direction of film growth as a result of the impingement between two crystalline regions.

signing the development of the preferred crystallographic orientation.

To unravel the origin of the preferred crystallographic orientation, high-resolution TEM analysis was performed on the 2.00 μm thick film (Fig. 4). Similar to SEM observations (Fig. 1b), cross-sectional TEM images show that the cone-shaped regions exhibit a feather-like morphology composed of nano-branches (Fig. 2a and Fig. 4a-c). In addition, the formation of rings in the SAED pattern shown in Fig. 2b points-out the polycrystalline and non-preferentially oriented nature of the cone-shaped regions. This is in line with the nearly constant values detected in both the pole figure and average intensity of the 2.00 μm thick film (Fig. 3a-b). However, a different situation occurs when analyzing individual nano-branches forming the crystalline cone-shaped regions. The high-resolution TEM image acquired at the center of a nano-branch (Fig. 4d-e) and its corresponding Fast Fourier transform (FFT) pattern (Fig. 4f) indicate that the core of the nano-branch is monocrystalline, with the (110) crystallographic planes oriented perpendicular to the growth direction of the nano-branch.

These results shed light on the origin of the development of a preferred crystallographic orientation with increasing film thickness, revealed by pole figure analysis. Indeed, as the film thickness increases, the crystalline regions come into contact with each other. This process inhibits the in-plane growth of crystalline nano-branches close to the generatrix of the cone-shaped regions, which is reflected in the fact that the boundary between two crystalline regions is normal to the substrate (Fig. 5a). Hence, while the nano-branches closer to the cone generatrix are progressively blocked with increasing film thickness, the nano-branches growing close to the cone axis (i.e., in the growth direction of the film) continue their growth (Fig. 5). Moreover, looking at the TEM images in Figs. 2a and 4a and SEM image in Fig. 5a, it is clear that primary nano-branches produce secondary nano-branches, among which those oriented close to the direction of film growth are not constrained, continue to grow and contribute to the development of the preferred orientation (Fig. 5b). In addition, there is also evidence that the axis of the nano-branches can be forced to bent to some extent due to the lateral confinement (Fig. 5b). All these effects, which are a consequence of the impingement between crystalline regions, triggers the development of the preferred orientation of the (110) crystallographic planes in the growth direction of the film.

4. Conclusions

In summary, we demonstrated the occurrence of the crystalline/amorphous competitive growth phenomenon in sputter-deposited Zr-V films with 83 at% V. We showed that, in these dual-phase alloys, the ratio between the crystalline and amorphous phases increases with film thickness due to the progressive overgrowth of the amorphous phase by the crystalline one. Pole figure analysis revealed that, as the film thickness increases, a preferred orientation of the (110) crystallographic planes in the growth direction of the film develops. We explained this process by relying on high-resolution TEM analysis showing that the core of the nano-branches forming the crystalline regions grow (110)-oriented. Consequently, we attributed the development of the (110)-preferred orientation to the favored selection of nano-branches growing near the film growth direction, triggered by the impingement between the crystalline regions. Our results shed new light on the structural and microstructural evolution in Zr-V thin films exhibiting crystalline/amorphous competitive growth, and could serve as a platform for understanding the growth mechanisms in other systems in which this phenomenon occurs.

Declaration of Competing Interest

The authors declare that they have no known competing financial interests or personal relationships that could have appeared to influence the work reported in this paper.

Data Availability

Data will be made available on request.

Acknowledgements

The Daυm competence center of IJL is deeply acknowledged for access to UHV magnetron sputtering deposition facility.

References

[1] F.C. Li, T. Liu, J.Y. Zhang, S. Shuang, Q. Wang, A.D. Wang, J.G. Wang, Y. Yang, Amorphous–nanocrystalline alloys: fabrication, properties, and applications, Mater. Today Adv. 4 (2019) 100027, https://doi.org/10.1016/j.mtadv.2019.100027.

[2] G. Wu, K.-C. Chan, L. Zhu, L. Sun, J. Lu, Dual-phase nanostructuring as a route to high-strength magnesium alloys, Nature 545 (2017) 80–83, https://doi.org/10.1038/nature21691.
[3] G. Wu, C. Liu, L. Sun, Q. Wang, B. Sun, B. Han, J.-J. Kai, J. Luan, C.T. Liu, K. Cao, Y. Lu, L. Cheng, J. Lu, Hierarchical nanostructured aluminum alloy with ultrahigh strength and large plasticity, Nat. Commun. 10 (2019) 5099, https://doi.org/10.1038/s41467-019-13087-4.
[4] K. Ming, Z. Zhu, W. Zhu, B. Fang, B. Wei, P.K. Liaw, X. Wei, J. Wang, S. Zheng, Enhancing strength and ductility via crystalline-amorphous nanoarchitectures in TiZr-based alloys, Sci. Adv. 8 (2022) eabm2884, https://doi.org/10.1126/sciadv.abm2884.
[5] X. Li, J. Zhou, L. Shen, B. Sun, H. Bai, W. Wang, Exceptionally High Saturation Magnetic Flux Density and Ultralow Coercivity via an Amorphous–Nanocrystalline Transitional Microstructure in an FeCo-Based Alloy, Adv. Mater. (2022) 2205863, https://doi.org/10.1002/adma.202205863.
[6] C. Wang, T. Wang, S. Yu, B. Li, L. Cao, G. Zhang, Unexpected thermal stability of dual-phase amorphous-nanocrystalline Al0.74Mo0.26 alloy film prepared by annealing-induced crystallization, Appl. Surf. Sci. 543 (2021) 148787, https://doi.org/10.1016/j.apsusc.2020.148787.
[7] A. Khalajhedayati, Z. Pan, T.J. Rupert, Manipulating the interfacial structure of nanomaterials to achieve a unique combination of strength and ductility, Nat. Commun. 7 (2016) 10802, https://doi.org/10.1038/ncomms10802.
[8] C.M. Grigorian, T.J. Rupert, Thick amorphous complexion formation and extreme thermal stability in ternary nanocrystalline Cu-Zr-Hf alloys, Acta Mater. 179 (2019) 172–182, https://doi.org/10.1016/j.actamat.2019.08.031.
[9] A. Borroto, S. Bruyère, S. Migot, J.F. Pierson, T. Gries, F. Mücklich, D. Horwat, Controlling surface morphology by nanocrystalline/amorphous competitive self-phase separation in thin films: Thickness-modulated reflectance and interference phenomena, Acta Mater. 181 (2019) 78–86, https://doi.org/10.1016/j.actamat.2019.09.036.
[10] A. Borroto, A.C. García-Wong, S. Bruyère, S. Migot, D. Pilloud, J.F. Pierson, F. Mücklich, D. Horwat, Composition-driven transition from amorphous to crystalline films enables bottom-up design of functional surfaces, Appl. Surf. Sci. 538 (2021) 148133, https://doi.org/10.1016/j.apsusc.2020.148133.
[11] A. Borroto, S. Bruyère, S. Migot, J.F. Pierson, F. Mücklich, D. Horwat, Growth kinetics and origin of residual stress of two-phase crystalline-amorphous nanostructured films, J. Appl. Phys. 129 (2021) 145301, https://doi.org/10.1063/5.0044029.
[12] P. Zeman, S. Haviar, M. Červená, Self-formation of dual glassy-crystalline structure in magnetron sputtered W–Zr films, Vacuum 187 (2021) 110099, https://doi.org/10.1016/j.vacuum.2021.110099.
[13] Q. Liebgott, A. Borroto, Z. Fernández-Gutiérrez, S. Bruyère, F. Mücklich, D. Horwat, Deposition rate controls nucleation and growth during amorphous/nanocrystalline competition in sputtered Zr-Cr thin films, J. Alloy. Compd. 936 (2023) 168258, https://doi.org/10.1016/j.jallcom.2022.168258.
[14] Vl Kolkovsky, J.-U. Schmidt, S. Döring, Electrical and structural properties of direct current magnetron sputtered amorphous TiAl thin films, Thin Solid Films 669 (2019) 169–173, https://doi.org/10.1016/j.tsf.2018.10.033.
[15] V. Brien, P. Miska, B. Bolle, P. Pigeat, Columnar growth of ALN by r.f. magnetron sputtering: Role of the {101¯3} planes, J. Cryst. Growth 307 (2007) 245–252, https://doi.org/10.1016/j.jcrysgro.2007.06.013.
[16] R. Gago, M. Vinnichenko, A. Redondo-Cubero, Z. Czigány, L. Vázquez, Surface Morphology of Heterogeneous Nanocrystalline Rutile/Amorphous Anatase TiO_2 Films Grown by Reactive Pulsed Magnetron Sputtering, Plasma Process. Polym. 7 (2010) 813–823, https://doi.org/10.1002/ppap.200900182.
[17] M.J. Burch, J. Li, D.T. Harris, J.-P. Maria, E.C. Dickey, Mechanisms for microstructure enhancement in flux-assisted growth of barium titanate on sapphire, J. Mater. Res. 29 (2014) 843–848, https://doi.org/10.1557/jmr.2014.59.
[18] J. Koh, Y. Lee, H. Fujiwara, C.R. Wronski, R.W. Collins, Optimization of hydrogenated amorphous silicon *p–i–n* solar cells with two-step *i* layers guided by real-time spectroscopic ellipsometry, Appl. Phys. Lett. 73 (1998) 1526–1528, https://doi.org/10.1063/1.122194.
[19] R.W. Collins, A.S. Ferlauto, G.M. Ferreira, C. Chen, J. Koh, R.J. Koval, Y. Lee, J. M. Pearce, C.R. Wronski, Evolution of microstructure and phase in amorphous, protocrystalline, and microcrystalline silicon studied by real time spectroscopic ellipsometry, Sol. Energy Mater. Sol. Cells 78 (2003) 143–180, https://doi.org/10.1016/S0927-0248(02)00436-1.
[20] A. Tomasi, B. Paviet-Salomon, Q. Jeangros, J. Haschke, G. Christmann, L. Barraud, A. Descoeudres, J.P. Seif, S. Nicolay, M. Despeisse, S. De Wolf, C. Ballif, Simple processing of back-contacted silicon heterojunction solar cells using selective-area crystalline growth, Nat. Energy 2 (2017) 1–8, https://doi.org/10.1038/nenergy.2017.62.
[21] K. Mašek, F. Šutara, T. Skála, J. Drbohlav, K. Veltruská, V. Matolín, X-ray photoelectron spectroscopy and static secondary ion mass spectroscopy study of activation mechanism of Zr–V low activation temperature nonevaporable getter films, J. Vac. Sci. Technol. A: Vac., Surf., Films 21 (2003) 797–805, https://doi.org/10.1116/1.1562175.
[22] V. Matolín, J. Drbohlav, K. Mašek, Mechanism of non-evaporable getter activation XPS and static SIMS study of Zr44V56 alloy, Vacuum 71 (2003) 317–322, https://doi.org/10.1016/S0042-207X(02)00756-X.
[23] S. Fabík, V. Cháb, V. Dudr, K. Mašek, K.C. Prince, F. Šutara, K. Veltruská, N. Tsud, M. Vondráček, V. Matolín, Activation of binary Zr–V non-evaporable getters: a soft X-ray photoemission study of carbide formation, Surf. Sci. 566–568 (2004) 1246–1249, https://doi.org/10.1016/j.susc.2004.06.138.
[24] V. Matolín, K. Mašek, I. Matolínová, T. Skála, K. Veltruská, XPS and SIMS study of the ageing mechanism of Zr–V non-evaporable getter films, Appl. Surf. Sci. 235 (2004) 202–206, https://doi.org/10.1016/j.apsusc.2004.05.125.
[25] V. Matolín, V. Dudr, S. Fabík, V. Cháb, K. Mašek, I. Matolínová, K.C. Prince, T. Skála, F. Šutara, N. Tsud, K. Veltruská, Activation of binary Zr–V non-evaporable getters: synchrotron radiation photoemission study, Appl. Surf. Sci. 243 (2005) 106–112, https://doi.org/10.1016/j.apsusc.2004.09.049.
[26] M.V. Lototsky, V.A. Yartys, Ye.V. Klochko, V.N. Borisko, R.I. Starovoitov, V. M. Azhazha, P.N. V'yugov, Applications of Zr–V hydrogen getters in vacuum-plasma devices: Phase-structural and hydrogen sorption characteristics, J. Alloy. Compd. 404–406 (2005) 724–727, https://doi.org/10.1016/j.jallcom.2005.02.086.
[27] S. Lemettre, S. Hammami, A. Bosseboeuf, P. Coste, J. Moulin, In-situ electrical characterization of co-evaporated Zr–Ti, Zr–V and Zr–Co thin getter films during thermal activation, Micro Technol. 25 (2019) 4091–4096, https://doi.org/10.1007/s00542-019-04412-4.
[28] D.B. Miracle, D.V. Louzguine-Luzgin, L.V. Louzguina-Luzgina, A. Inoue, An assessment of binary metallic glasses: correlations between structure, glass forming ability and stability, Int. Mater. Rev. 55 (2010) 218–256, https://doi.org/10.1179/095066010X12646898728200.
[29] J. Cui, C. Guo, L. Zou, C. Li, Z. Du, Thermodynamic modeling of the V–Zr system supported by key experiments, Calphad 53 (2016) 122–129, https://doi.org/10.1016/j.calphad.2016.03.008.
[30] J.A. Thornton, High Rate Thick Film Growth, Annu. Rev. Mater. Sci. 7 (1977) 239–260, https://doi.org/10.1146/annurev.ms.07.080177.001323.
[31] A. Anders, A structure zone diagram including plasma-based deposition and ion etching, Thin Solid Films 518 (2010) 4087–4090, https://doi.org/10.1016/j.tsf.2009.10.145.